

## Structure and compressibility of Fe-bearing Al-phase D

GIACOMO CRINITI<sup>1,\*</sup>, TAKAYUKI ISHII<sup>2,†</sup>, ALEXANDER KURNOSOV<sup>1</sup>, KONSTANTIN GLAZYRIN<sup>3</sup>,  
RACHEL J. HUSBAND<sup>3</sup>, AND TIZIANA BOFFA BALLARAN<sup>1</sup>

<sup>1</sup>Bayerisches Geoinstitut, University of Bayreuth, 95440 Bayreuth, Germany

<sup>2</sup>Center for High Pressure Science and Technology Advanced Research, Beijing, 100094, China

<sup>3</sup>Deutsches Elektronen-Synchrotron DESY, Notkestr. 85, 22607 Hamburg, Germany

### ABSTRACT

Due to its large thermal stability, Al-phase D, the  $(\text{Al,Fe}^{3+})_2\text{SiO}_6\text{H}_2$  member of the dense hydrous magnesium silicate (DHMS) phase D, may survive along hot subduction geotherms or even at ambient mantle temperatures in the Earth's transition zone and lower mantle, therefore potentially playing a major role as a water reservoir and carrier in the Earth's interior. We have investigated the crystal structure and high-pressure behavior of Fe-bearing Al-phase D with a composition of  $\text{Al}_{1.53(2)}\text{Fe}_{0.22(1)}\text{Si}_{0.86(1)}\text{O}_6\text{H}_{3.33(9)}$  by means of single-crystal X-ray diffraction. While the structure of pure Al-phase D ( $\text{Al}_2\text{SiO}_6\text{H}_2$ ) has space group  $P6_3/mcm$  and consists of equally populated and half-occupied  $(\text{Al,Si})\text{O}_6$  octahedra, Fe-incorporation in Al-phase D seems to induce partial ordering of the cations over the octahedral sites, resulting in a change of the space group from  $P6_3/mcm$  to  $P6_322$  and in well-resolved diffuse scattering streaks observed in X-ray images. The evolution of the unit-cell volume of Fe-bearing Al-phase D between room pressure and 38 GPa, determined by means of synchrotron X-ray diffraction in a diamond anvil cell, is well described by a third-order Birch-Murnaghan equation of state having an isothermal bulk modulus  $K_{T0} = 166.3(15)$  GPa and first pressure derivative  $K'_{T0} = 4.46(12)$ . Above 38 GPa, a change in the compression behavior is observed, likely related to the high-to-low spin crossover of octahedrally coordinated  $\text{Fe}^{3+}$ . The evolution of the unit-cell volume across the spin crossover was modeled using a recently proposed formalism based on crystal-field theory, which shows that the spin crossover region extends from approximately 30 to 65 GPa. Given the absence of abrupt changes in the compression mechanism of Fe-bearing Al-phase D before the spin crossover, we show that the strength of H-bonds and likely their symmetrization do not greatly affect the elastic properties of phase D solid solutions, independently of their compositions.

**Keywords:** DHMS, phase D, X-ray diffraction, equation of state, spin crossover

### INTRODUCTION

The stability of dense hydrous magnesium silicates (DHMS) at high-pressure and high-temperature conditions has been extensively studied for more than 20 years, as these phases can potentially carry and recycle water from Earth's surface to its deep interior (e.g., Frost 2006; Nishi et al. 2014; Ohtani et al. 2014). The crystal structure of DHMS generally consists of hexagonal closest-packed (*hcp*) layers of O atoms with Mg and Si occupying interstitial octahedral and tetrahedral sites, respectively. However, in phase D and phase H, which are stable under mantle transition zone and lower mantle conditions, Si displays octahedral coordination, allowing partial (Yang et al. 1997) or complete (Bindi et al. 2014) mixing with Mg to take place. Al incorporation in the crystal structures of these two phases further promotes cation mixing at octahedral sites and enhances their thermal stability, allowing Al-bearing phase D and phase H to potentially survive along hot subduction geotherms or even at ambient mantle temperatures in the transition zone and lower

mantle (Ohira et al. 2014; Pamato et al. 2015).

In the end-member Mg-phase D (space group  $P\bar{3}1m$ ), with nominal composition  $\text{MgSi}_2\text{O}_6\text{H}_2$ , Mg and Si occupy distinct octahedral sites, named M1 and M2, respectively, located on alternated interstitial layers of the oxygen *hcp* sublattice (Yang et al. 1997). M2 octahedra are connected with one another through one edge and to M1 octahedra through vertices, while M1 octahedra are separated from one another and share vertices with M2 octahedra (Online Materials<sup>1</sup> Fig. S1a). The remaining two octahedral sites, i.e., M3 and M4, share faces with M2 and M1, respectively, and are nominally vacant in Mg-phase D. Previous studies showed that the crystal structure of phase D becomes progressively disordered in the proximity of its Al-end-member (Boffa Ballaran et al. 2010; Pamato et al. 2015). As Al is incorporated in the structure of phase D via the  $\text{Mg}^{2+} + \text{Si}^{4+} = 2\text{Al}^{3+}$  substitution, not only this cation substitutes in both M1 and M2, but also causes a partial redistribution of the cations in the M3 and M4 sites. In an Al-rich phase D sample having  $\text{Mg} + \text{Fe} = 0.3$  atoms per formula unit, cation disordering was observed in the form of partially occupied, but not equally populated M2 and M3 sites, while M1 showed full occupancy and M4 appeared vacant (Boffa Ballaran et al. 2010). In Mg- and Fe-free

\* E-mail: giacomo.criniti@uni-bayreuth.de. Orcid 0000-0002-9414-523X

† Present address: Institute for Planetary Materials, Okayama University, Misasa, Japan.

Al-phase D (Online Materials<sup>1</sup> Fig. S1b), nominally  $\text{Al}_2\text{SiO}_6\text{H}_2$ , the distribution of Al and Si over the cation sites is completely random (Pamato et al. 2015) and, as a consequence, the crystal symmetry increases from  $P\bar{3}1m$  to  $P6_3/mcm$ . From the structural refinement of Al-phase D, it was also found that the Pauling bond strength of O atoms is +1.42, which is significantly smaller than in Mg-phase D (i.e., +1.67) and suggests that stronger covalent bonds O-H and hydrogen bonds (or H-bonds)  $\text{O}\cdots\text{H}$  are formed as a result of Al substitution and cation disordering.

In a recent publication, the pressure induced symmetrization of H-bonds was reported in  $\text{CaCl}_2$ -structured  $\delta$ -AlOOH (Sano-Furukawa et al. 2018). Phase  $\delta$  is stable in hydrous basaltic systems at lower mantle pressures, where it forms solid solutions with  $\text{MgSiO}_4\text{H}_2$  phase H (Ohira et al. 2014; Liu et al. 2019). Owing to its strong symmetric H-bonds, the bulk modulus of  $\delta$ -AlOOH was found to substantially increase across the symmetrization (Sano-Furukawa et al. 2009; Satta et al. 2021), to the point that the presence of  $\delta$ -H solid solutions in hydrous subducted basalt can produce a 1.5% increase in its seismic velocities with respect to dry basalt at topmost lower mantle pressures (Satta et al. 2021). While it is still controversial whether a pressure induced H-bond symmetrization takes place in Mg-phase D and whether it affects its elastic properties (Hushur et al. 2011; Rosa et al. 2013), H-bonds in Al-phase D are known to be stronger than in Mg-phase D already at ambient conditions (Pamato et al. 2015). However, previous experimental studies on the compressibility of phase D were conducted only on samples rich in Mg, hampering our understanding of how strongly the H-bonds affect the bulk modulus systematics of phase D solid solutions and whether the H-bond symmetrization influences the high-pressure structural evolution of phase D, similarly to what has been observed for phase  $\delta$ -H. To assess this possibility, we investigated the crystal structure of single-crystal Fe-bearing Al-phase D at ambient conditions using X-ray diffraction, with particular emphasis on the relation between cation disordering and strength of H-bonds. Additionally, the high-pressure behavior of Fe-bearing Al-phase D was determined for the first time using diamond anvil cells (DAC) and synchrotron X-ray diffraction, providing insights into the relation among H-bond symmetrization, spin state of Fe, and elasticity of phase D solid solutions at high pressure.

## EXPERIMENTAL METHODS

### Sample synthesis and characterization

Fe-bearing Al-Phase D was synthesized at 27 GPa and 1673 K in the 15-MN Kawai-type multi-anvil apparatus with the Osugi-type (DIA) guide block system, IRIS-15, installed at the Bayerisches Geoinstitut, University of Bayreuth (Ishii et al. 2016, 2019; Liu et al. 2017). The starting material, consisting of a finely ground mixture of  $\text{SiO}_2$ ,  $\text{Al}(\text{OH})_3$ , and  $\text{Fe}_2\text{O}_3$  in the molar proportion 2:6:1, was loaded in a Pt tube capsule that was then sealed by welding. A  $\text{LaCrO}_3$  heater was inserted in a  $\text{Cr}_2\text{O}_3$ -doped MgO octahedron with 7 mm edge length, which served as pressure medium. WC cubes having 3 mm truncated edge length were employed for high-pressure generation and compressed to a load of 13 MN. The sample was heated for 3 h, quenched by cutting the electric power supply and slowly decompressed to ambient conditions in 12 h. The recovered sample consisted of coexisting Fe-bearing Al-phase D (light-brown color and up to approximately 150  $\mu\text{m}$  in their longest directions) and  $\delta$ -(Al,Si,Fe)OOH (brown-blue pleochroism under polarized light and up to 200  $\mu\text{m}$  in size), identified by single-crystal X-ray diffraction.

Inclusion-free samples of Fe-bearing Al-phase D were embedded in epoxy for textural and chemical analyses. Backscattered electron (BSE) images were acquired

using a LEO Gemini 1530 scanning electron microscope (SEM) and showed that the samples are chemically homogeneous. The chemical compositions of several phase D crystals were determined using a JEOL JXA-8200 electron probe micro-analyzer (EPMA) operated at an acceleration voltage of 15 kV and a beam current of 5 nA. Enstatite was used as a standard for Si, corundum for Al and metal iron for Fe, while the  $\text{H}_2\text{O}$  concentration was determined as the difference between 100% and the observed EPMA totals. The average composition was calculated from a total of 51 measurements on 6 different crystals and resulted to be  $\text{Al}_{1.53(2)}\text{Fe}_{0.22(1)}\text{Si}_{0.86(1)}\text{O}_6\text{H}_{3.33(9)}$ , where the numbers between parentheses indicate one standard deviation on the last digit. To determine the valence of Fe in the sample, Mössbauer spectroscopy (MS) measurements were performed on a mosaic of several hand-picked single crystals of Fe-bearing Al-phase D using a constant acceleration spectrometer in combination with a point  $^{57}\text{Co}$  source (McCammon 1994). A Ta mask with a 500  $\mu\text{m}$  hole was applied in front of the sample because of the limited amount of material available. The Mössbauer spectrum of Fe-bearing Al-phase D (Fig. 1) was collected over 7 days and fitted with one asymmetric Lorentzian doublet using MossA (Prescher et al. 2012). The determined isomer shift (IS) of 0.34(2) mm/s and quadrupole splitting (QS) of 0.63(2) mm/s are consistent with those of  $\text{Fe}^{3+}$  found in previous studies for Fe-Al-bearing Mg-phase D samples (Chang et al. 2013; Wu et al. 2016).

### Single-crystal X-ray diffraction at ambient conditions

Single crystals of Fe-bearing Al-phase D were observed under a polarizing microscope and selected for X-ray diffraction measurements based on their sharp optical extinction and the absence of visible twinning and inclusions. A crystal with dimensions  $120 \times 70 \times 60 \mu\text{m}^3$  was analyzed at ambient conditions using a Huber single-crystal diffractometer equipped with a point detector and operated by the SINGLE software (Angel and Finger 2011) for precise and accurate lattice parameters determination. The diffractometer employed a  $\text{MoK}\alpha$  tube operated at 50 kV and 40 mA. Typical diffraction profiles measured upon  $\omega$ -scan rotations showed full-width half maxima (FWHM) ranging between  $0.05^\circ$  and  $0.08^\circ$ . The unit-cell parameters were determined by vector least-square fitting of 22 reflections, each

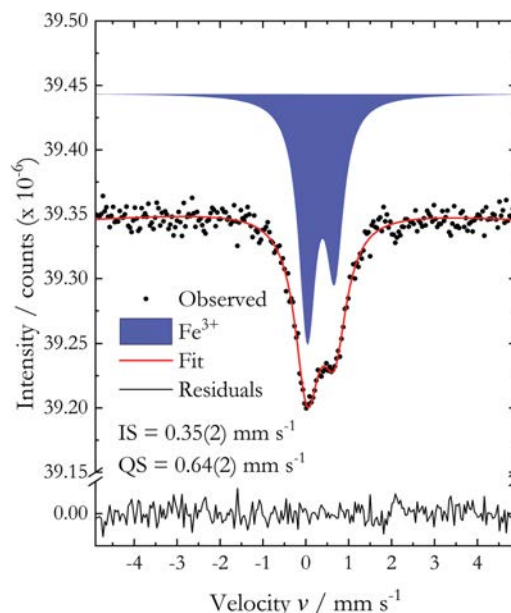


**FIGURE 1.** Mössbauer spectrum of Fe-bearing Al-phase D. The spectrum was fit to a single Lorentzian doublet that was assigned to octahedrally coordinated  $\text{Fe}^{3+}$  (blue area). The asymmetry of the doublet likely arises from the fact that the sample consisted of a mosaic of few single crystals, rather than a fine powder with completely randomly oriented crystallites. Although the candidate  $P6_322$  and  $P\bar{3}1m$  space groups have multiple octahedral sites occupied by  $\text{Fe}^{3+}$ , we used a single Lorentzian doublet to fit the transmission spectrum due to the non-distorted shape and very similar volume of octahedra (similar crystal field).

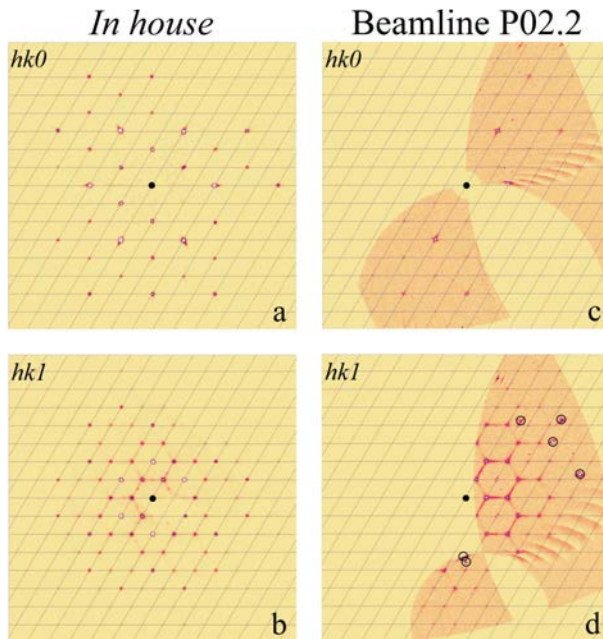


**FIGURE 2.** Unwarp images of the reciprocal space of Fe-bearing Al-phase D samples obtained from single-crystal X-ray diffraction measurements in-house (a and b) and at the ECB P02.2 in Hamburg (c and d). When  $l = 2n$  (e.g.,  $hk0$  in a and c), no diffuse scattering is observed between neighboring reflections. When  $l = 2n + 1$  (e.g.,  $hk1$  in b and d) diffuse scattering streaks are observed between neighboring reflection for which  $h - k \neq 3n$ . The black dot at the center of each image denotes the origin of the plane in reciprocal space. Black circles in d denote reflections from the diamond anvil where the crystal was placed to be measured at the ECB P02.2.

centered in 8-positions (King and Finger 1979; Ralph and Finger 1982) yielding  $a = 4.74653(13) \text{ \AA}$ ,  $c = 4.29002(19) \text{ \AA}$ , and  $V = 83.703(6) \text{ \AA}^3$ . Intensity data for the same crystal were collected on a Xcalibur diffractometer (Rigaku, Oxford Diffraction) equipped with a Sapphire2 CCD detector and graphite-monochromatized MoK $\alpha$  radiation operated at 50 kV and 40 mA. X-ray scans were acquired upon  $\omega$ -rotations of the crystal up to  $2\theta_{\max} = 90^\circ$  with exposure times of 5 or 15 s at low and high  $2\theta$ , respectively. CrisAlysPro (Rigaku, Oxford Diffraction) was used for data processing, which included integration of intensities, correction for Lorentz and polarization factors, frame scaling and empirical absorption correction based on spherical harmonics. The obtained average redundancy of unique reflections was 6.2 in the Laue class  $3m$ . The space groups  $P6_3$ ,  $P6_3/m$ , and  $P6_322$  were compatible with the analysis of systematic absences. In addition, we also tested a structural model having space group  $P\bar{3}1m$ , i.e., the same as Mg-phase D. No evidence for polytypism along the  $c^*$  axis was found through the analysis of unwarp images of reciprocal planes  $h0l$  and  $h1l$ . However, strong diffuse scattering was observed in the  $hk1$ ,  $hk3$ , etc., reciprocal planes (Fig. 2), as discussed later. For the hexagonal space groups, structure solutions were performed using the dual-space algorithm SHELXT (Sheldrick 2015b) and each structural model was refined against  $F^2$  using SHELXL (Sheldrick 2015a) in the ShelXle GUI (Hübschle et al. 2011). As Al-phase D has only partially occupied cationic sites, in our structural refinement we assumed Al, Si, and Fe to be completely disordered in each site and their cation fractions to be  $X_{\text{Al}}: X_{\text{Si}}: X_{\text{Fe}} = 0.59: 0.33: 0.08$ , as determined by EPMA. The total occupancy of each site was then refined independently. Mean atomic numbers (m.a.n.) for each site were finally calculated by multiplying the site occupancy factors obtained in our structural models by the fraction  $X_i$  of each cation ( $i = \text{Al, Si, Fe}$ ) and its atomic number. In their final cycles, structural refinements for all space groups resulted in discrepancy factors (R1) not exceeding 5.1%, with the exception of  $P6_3/m$  (R1 >20%). Further details on the structural models with space groups  $P6_322$  and  $P\bar{3}1m$  are provided in the Online Materials' Crystallographic Information File (CIF). An attempt was also made for the  $P6_322$  space group to refine the distribution of cations among the different crystallographic sites without constraining the cation

fraction but simply using restraints on the chemical composition, to shed light on potential order of Fe vs. Al + Si. However, due to the lack of information on the total occupancy of the sites, which are only partially occupied, the resulting model was less stable than the one described above, showing an increased R1 = 8.6% and negative occupancy factors for some of the sites. Therefore, this structural model was discarded.

### Single-crystal X-ray diffraction at high pressure

To study the compressibility of Fe-bearing Al-phase D, we performed single-crystal X-ray diffraction measurements in a DAC up to  $\sim 52$  GPa at the Extreme Conditions Beamline (ECB) P02.2 of PETRA III (Hamburg, Germany). Two runs were performed using either  $8 \times 3 \mu\text{m}^2$  or  $2 \times 2 \mu\text{m}^2$  (FWHM) X-ray beams of 25.6 and 42.7 keV, respectively, and a Perkin-Elmer XRD 1621 flat panel detector (Liermann et al. 2015). The sample-detector distance was calibrated using polycrystalline CeO $_2$  and the instrument parameters for single-crystal X-ray diffraction were refined using a natural enstatite standard. To generate high pressures, BX-90 type DACs capable to provide opening angles of up to  $90^\circ$  (Kantor et al. 2012) were employed together with Almax-Boehler diamonds (Boehler and De Hantsetters 2004) having culets of 350  $\mu\text{m}$  (run 1) or 250  $\mu\text{m}$  (run 2) in diameter and WC seats with large ( $\sim 80^\circ$ ) opening angle. According to the target pressure of each run, i.e.,  $\sim 38$  GPa in run 1 and 52 GPa in run 2, a Re gasket was indented to 53 or 35  $\mu\text{m}$ , respectively, and laser-drilled to create the sample chamber. The same high-quality single-crystal of Fe-bearing Al-phase D of approximately  $20 \times 10 \times 10 \mu\text{m}^3$  was employed for both runs. A ruby sphere serving as the pressure standard (Shen et al. 2020) and a piece of Au for fine alignment of the DAC under the X-ray beam were also placed in the sample chamber next to the crystal. Pre-compressed He at 0.13 GPa was loaded as a quasi-hydrostatic pressure-transmitting medium in both runs using the gas loading system at the Bayerisches Geoinstitut, University of Bayreuth (Kurnosov et al. 2008). Pressure was increased online using a gas-driven membrane up to approximately 38 GPa (run 1) and 52 GPa (run 2) with steps of 2–4 GPa. X-ray scans were collected upon continuous omega rotation of the DAC between  $-35^\circ$  and  $+35^\circ$ , with steps of  $0.5^\circ$  and an exposure time of 1 s. Data analysis was performed using CrisAlysPro (Rigaku, Oxford Diffraction) following the same procedure described for in-house measurements at room pressure. In addition to high-pressure measurements, another single-crystal grain with a diameter of  $<20 \mu\text{m}$  was measured at ambient conditions at the same beamline to analyze its crystal structure. To do so, the crystal was placed on the culet of a DAC without loading (i.e., the crystal was still at room pressure) and intensity data were collected following the same procedure employed for high-pressure measurements and described above. The measured unit-cell parameters for this crystal are  $a = 4.7469(4) \text{ \AA}$ ,  $c = 4.2891(6) \text{ \AA}$ , and  $V = 83.698(17) \text{ \AA}^3$ , which are in good agreement with in-house measurements. Further information can be found in the Online Materials' CIF.

## RESULTS AND DISCUSSION

### Crystal structure of Fe-bearing Al-Phase D

Three of the four structural models that were tested in this study, i.e.,  $P\bar{3}1m$ ,  $P6_3$ , and  $P6_322$ , yielded discrepancy factors (R1) of 5% or less. Models with  $P6_3$  and  $P6_322$  space groups resulted in identical structural parameters (atomic positions and site occupancy factors) within uncertainties. Therefore, only the higher symmetry space group  $P6_322$  will be discussed as it employs a smaller number of refined parameters. In Mg-bearing Al-phase D ( $P\bar{3}1m$  space group) analyzed by Boffa Ballaran et al. (2010), mean atomic numbers (m.a.n.) were calculated by allowing the site occupancy factor (s.o.f.) of a given site to be refined and subsequently multiplying the s.o.f. by the number of electrons of the scattering factors (for Si or Al) used to refine the occupancy at a given site. In this way, it was possible to quantify the amount of charge present in the M1, M2, and M3 sites of their phase D sample independently of the atomic species (i.e., Mg, Al, Si, or Fe) which were actually present at that site. Boffa Ballaran et al. (2010) found in that way that the m.a.n. of M2 is larger than that of M3, i.e., the adjacent octahedral site that shares faces with M2 perpendicular to the  $c$ -axis (Online Materials' Fig. S1a). The

cation distribution in their sample indicates that within a given unit cell there is a higher probability that Si and Al atoms occupy edge-sharing octahedra on the same interstitial layer rather than face-sharing sites on adjacent layers. Such mechanism seems to change, however, in the Fe-bearing Al-phase D sample analyzed in this study, as in both the  $P\bar{3}1m$  and  $P6_322$  space groups, all the cationic sites are partially occupied and have different m.a.n. It follows that Fe-bearing Al-phase D (Online Materials<sup>1</sup> Fig. S1c) represents an intermediate configuration between those of Mg-bearing (Online Materials<sup>1</sup> Fig. S1a) and Fe-free Al-phase D (Online Materials<sup>1</sup> Fig. S1b), where all sites are equally populated and have almost identical m.a.n.

The main differences between the  $P\bar{3}1m$  and  $P6_322$  models analyzed here consist of (1) a shift in the origin of the unit cell of the  $P6_322$  model by  $(1/3, 1/3, 1/4)$  with respect to that of the  $P\bar{3}1m$  model and (2) an apparently different distribution of the cations over the four crystallographic sites, resulting from different site occupancy factors and point group symmetry at the cation sites. In the trigonal model, the face-sharing octahedral sites M2 and M3 (Online Materials<sup>1</sup> Fig. S1a) exhibit m.a.n. of 8.10(7) and 4.27(5), respectively, while M1 and M4, which are also face-sharing, have m.a.n. equal to 9.71(8) and 2.50(7). In the space group  $P6_322$ , on the other hand, only three distinct cation sites exist (Online Materials<sup>1</sup> Fig. S1c). The first site has Wyckoff position  $2b$ , and its symmetry-equivalent coordinates are  $(0, 0, 1/4)$  and  $(0, 0, 3/4)$ , resulting in a chain of equivalent face-sharing octahedra aligned along the  $c$ -axis (Online Materials<sup>1</sup> Fig. S1c). The m.a.n. of the  $2b$  site is 6.23(7), meaning that its occupancy factor is approximately 43%. The other two sites have Wyckoff positions  $2c$  and  $2d$  and occupy the two remaining octahedral sites. These two sites lie at  $x = 1/3, y = 2/3$  and  $x = 2/3, y = 1/3$  of each interstitial layer, with their  $x$  and  $y$  coordinates swapping every interstitial layer. This means that in the first layer, where  $z = 1/4$ ,  $2c$  lies at  $(1/3, 2/3, 1/4)$  and  $2d$  at  $(2/3, 1/3, 1/4)$ , while in the second layer, having  $z = 3/4$ ,  $2c$  is located at  $(2/3, 1/3, 3/4)$  and  $2d$  at  $(1/3, 2/3, 3/4)$ . In other words,  $2c$  octahedra share edges with  $2d$  octahedra that are in the same interstitial layer and share faces with  $2d$  octahedra lying on adjacent layers, and vice versa (Online Materials<sup>1</sup> Fig. S1c). The m.a.n. refined for the  $2c$  and  $2d$  sites are 2.99(8) and 9.33(9), respectively, which correspond to site occupancy factors of approximately 21% and 65%, respectively. This configuration differs from that of Mg-bearing Al-phase D (Boffa Ballaran et al. 2010), where M2 and M3 sites are located on different interstitial layers (Online Materials<sup>1</sup> Fig. S1a) and may occur because of the smaller ionic radius of  $\text{Fe}^{3+}$  relative to  $\text{Mg}^{2+}$ , which favors cation mixing. For comparison, we determined the m.a.n. of the cation sites in the space group  $P6_322$  for the sample measured at ambient conditions at the ECB P02.2 and obtained values of 6.36(7), 3.58(7), and 9.19(12) for  $2b$ ,  $2c$  and  $2d$ , respectively, which are in fair agreement with those determined from in-house measurements. The total number of Al, Si, and Fe cations for 6 O atoms calculated from the site occupancy factors determined from in-house and synchrotron data falls within a  $\pm 2\%$  interval relative to that determined by EPMA. The m.a.n. of the  $2b$  and  $2d$  sites in the two samples are the same within mutual uncertainties, while that of  $2c$  is higher in the sample measured at the ECB P02.2. This could indicate, for instance, that the degrees of cation disordering in the two

samples are slightly different.

Hamilton (1965) proposed a statistical test to assess whether the increase in the number of parameters between similar structural models produces a statistically significant improvement in the quality of the structural refinement. One condition to apply Hamilton's test is that the number of unique reflections in the two structural models is the same. This condition is not fulfilled by the space groups  $P6_322$  and  $P\bar{3}1m$  since they belong to different Laue classes and thus have different averaging rules. If the test is conducted while neglecting this condition, the hypothesis that the hexagonal model better represents the actual atomic configuration is rejected at a 0.005 significance level, meaning that the trigonal model should be used. A way to properly apply Hamilton's test would be to compare the hexagonal and trigonal structural models refined against non-merged data sets. In this case, the number of reflections is the same by definition as long as the reflection file in the two refinements is the same. This procedure yielded a slightly larger weighted R factor for the  $P\bar{3}1m$  model relative to the  $P6_322$  model. Therefore, in the case of non-merged intensities, the hypothesis that the hexagonal model better represents the actual atomic configuration cannot be rejected. The apparent contradiction between the two approaches to Hamilton's test prevents us from drawing any conclusion on which model is the most suitable to describe the structure of Fe-bearing Al-phase D.

Like previously analyzed Al-rich phase D samples, we observed no long-range octahedral distortion, with M-O distances being all identical to each other within uncertainties. As pointed out by Boffa Ballaran et al. (2010), this does not exclude that distortions can arise at the local scale due to the fact that in each given unit cell only three of the six cationic sites must be occupied so that charge balance is preserved. Boffa Ballaran et al. (2010) ruled out the possibility of cation ordering in their Mg-bearing Al-phase D sample due to the absence of additional peaks in the X-ray diffraction patterns that would indicate the presence of a superstructure. However, weak diffuse scattering was observed in electron diffraction patterns, suggesting that short range ordering of the cations might exist at the nanoscale. Our Fe-bearing Al-phase D sample, on the other hand, shows much stronger diffuse scattering streaks that are well visible in X-ray diffraction images. Unwarps obtained by integration of X-ray scans collected both in-house and at the beamline P02.2 show that diffuse scattering is localized in reciprocal planes having odd  $l$  indices and only between reflections that satisfy the conditions  $h - k = 3n + 1$  or  $h - k = 3n + 2$ , where  $n$  is an integer number (Fig. 2). If we consider the space group  $P6_322$ , the first condition rules out any influence of the cation site  $2b$ , for which the reflection conditions of any  $hkl$  reflection is  $l = 2n$ . When  $h - k = 3n$  and  $l = 2n + 1$ , i.e., when the contribution of Wyckoff positions  $2c$  and  $2d$  to the structure factor is null, no diffuse scattering streaks are observed around the peaks. Therefore, diffuse scattering must originate from the short-range ordering of cations in  $2c$  and  $2d$ . On the other hand, in the trigonal space group  $P\bar{3}1m$ , there is no extinction rule for any atomic position due to the absence of additional translational symmetry. Therefore, it would be difficult to reconcile such a peculiar type of diffuse scattering with partial ordering of cations over the four available octahedral sites of the trigonal structure. Our analysis of diffuse

scattering thus suggests that the hexagonal space group is more suitable to describe the crystal structure and partial ordering of Fe-bearing Al-phase D. Owing to the difference in wavelength between in-house and synchrotron experiments, the types of diffuse scattering observed in the diffraction patterns have slightly different features, as short wavelengths can probe displacements at higher resolution. In fact, in the unwarps from synchrotron measurements, homogeneous streaks are found to connect the main reflections (Fig. 2d), while weak additional peaks appear at 1/2 or 1/3 fractional positions between the main reflections in the unwarps obtained from in-house measurements (Fig. 2b).

From our structural model, the bond valence analysis of O atoms can also be performed following the example of Pamato et al. (2015). We employed the computer software SPuDS (Lufaso and Woodward 2001) to compute the effective charge of each bond using the interatomic distances and site occupancy factors for each cation site that were obtained from our structural models. Note that because Al, Si, and Fe coexist in the same crystallographic sites, the contribution of each cation to the bond valence was weighted by their abundances,  $X_i$ , with  $i = \text{Al, Si, Fe}$ . We obtained an effective Pauling bond strength of +1.42 from both the  $P\bar{3}1m$  and  $P6_322$  models, which is identical to that determined for Al-phase D (Pamato et al. 2015) and is larger than those of Mg-rich compositions (Yang et al. 1997; Boffa Ballaran et al. 2010), supporting the hypothesis that cation disordering seems to induce stronger H bonds. In Mg-phase D, H-bonds are oriented along the edges of the vacant octahedral sites M3 and M4 (Online Materials' Fig. S1a), and their respective O...O distance is 2.675 Å (Yang et al. 1997). The O...O distance measured along the edges of octahedra of pure Al-phase D is 2.655(3) Å (Pamato et al. 2015), while for Fe-bearing Al-phase D, it is 2.665(1) Å, which are both smaller than in Mg-phase D since the spacing between O layer stacked perpendicular to the  $c$ -axis is also smaller. For comparison, O...O distances at ambient conditions in phase H and phase  $\delta$ -AlOOH are 2.461(4) and 2.5479(12) Å, respectively. Phase  $\delta$  is known to undergo H-bond disordering, followed by symmetrization, only when the O...O distances drop below the critical value of 2.443 Å (Meier et al. 2022). Therefore, it is unlikely that H-bonds in Al-phase D samples are symmetric, as they are approximately 4% larger than in phase  $\delta$  and 9% larger than the critical value of 2.443 Å.

### Equation of state of Fe-bearing Al-phase D

The evolution of the unit-cell volume and lattice parameters of Fe-bearing Al-phase D (Table 1) is displayed in Figure 3. A slight change in slope of the volume variation with pressure is observed above 38 GPa. For this reason the volume compression of Fe-bearing Al-phase D has been first modeled between room pressure and 38 GPa by fitting the pressure-volume ( $P$ - $V$ ) data set to both a third-order Birch-Murnaghan (BM3) (Birch 1947) and a Vinet (Vinet et al. 1989) equation of state (EOS). Following a similar approach, we use linearized BM3 and Vinet equations of state to fit the pressure evolution of individual unit-cell parameters ( $l$ ) of Fe-bearing Al-phase D, where  $V$  was substituted by the cube of the unit-cell parameters ( $l^3$ ),  $3K_{T0}$  by the axial modulus  $M_{l0}$  and  $3K'_{T0}$  by the axial modulus pressure derivative  $M'_{l0}$  (Angel 2000; Angel et al. 2014). Fitting was performed using the EosFit7c library implemented in EosFit7-

**TABLE 1.** Unit-cell parameters of Fe-bearing Al-phase D as a function of pressure

Run no.	$P$ (GPa)	$\sigma P$ (GPa)	$a$ (Å)	$\sigma a$ (Å)	$c$ (Å)	$\sigma c$ (Å)	$V$ (Å <sup>3</sup> )	$\sigma V$ (Å <sup>3</sup> )
1	0.35	0.02	4.7430	0.0005	4.2873	0.0003	83.525	0.017
1	1.02	0.02	4.7376	0.0004	4.2797	0.0005	83.186	0.015
1	3.35	0.08	4.7172	0.0004	4.2577	0.0004	82.050	0.015
1	5.25	0.07	4.7020	0.0006	4.2408	0.0005	81.196	0.016
1	7.56	0.08	4.6850	0.0004	4.2215	0.0003	80.247	0.016
1	10.66	0.08	4.6653	0.0004	4.2000	0.0003	79.165	0.016
1	13.64	0.16	4.6435	0.0004	4.1774	0.0003	78.007	0.012
1	16.44	0.04	4.6263	0.0006	4.1604	0.0004	77.112	0.016
1	18.36	0.09	4.6148	0.0004	4.1482	0.0003	76.506	0.011
1	19.16	0.08	4.6088	0.0004	4.1427	0.0003	76.205	0.012
1	21.41	0.08	4.5958	0.0004	4.1294	0.0003	75.535	0.011
1	24.66	0.23	4.5779	0.0005	4.1120	0.0003	74.631	0.013
1	27.66	0.11	4.5617	0.0005	4.0964	0.0004	73.821	0.014
1	30.50	0.12	4.5481	0.0007	4.0835	0.0004	73.152	0.017
1	32.79	0.09	4.5346	0.0006	4.0717	0.0004	72.509	0.015
1	35.32	0.10	4.5234	0.0007	4.0595	0.0005	71.935	0.017
1	37.92	0.09	4.5101	0.0007	4.0475	0.0005	71.302	0.018
2	5.84	0.02	4.6985	0.0002	4.2356	0.0013	80.98	0.02
2	9.23	0.02	4.6715	0.0002	4.2093	0.0013	79.55	0.02
2	23.07	0.04	4.5852	0.0003	4.1200	0.0020	75.01	0.04
2	33.30	0.05	4.5295	0.0005	4.0715	0.0018	72.36	0.03
2	40.75	0.05	4.4912	0.0006	4.0300	0.0020	70.43	0.04
2	42.42	0.05	4.4840	0.0007	4.0215	0.0020	70.05	0.04
2	45.96	0.05	4.4677	0.0006	4.0060	0.0020	69.27	0.03
2	49.41	0.08	4.4509	0.0006	3.9890	0.0020	68.47	0.04
2	52.41	0.05	4.4372	0.0006	3.9780	0.0030	67.91	0.05

Notes:  $P$  was calculated as the mean between values measured before and after XRD measurements using the ruby fluorescence shift (Shen et al. 2020), with  $\sigma P$  being their semi-difference.

GUI (Angel et al. 2014; Gonzalez-Platas et al. 2016) and the fitted parameters are reported in Table 2. The EOS parameters obtained from the two equation of states formalisms are identical within their mutual uncertainties (Table 2), resulting in complete overlaps of volume and linear EOSs in the pressure range considered (i.e., 0.0001–38 GPa). Therefore, for clarity, only the curves derived from the BM3 fits are shown in Figure 3. The fitted  $V_0$  is in very good agreement (i.e., within one standard deviation) with the unit-cell volume measured in-house and at the beamline P02.2 at room pressure. Alternative fits where the unit-cell volume and lattice parameters were fixed to the values measured at ambient conditions are also provided in Table 2, showing only slight variations in the refined moduli and pressure derivatives, typically identical within their mutual uncertainties. Consistently with previous observations on Mg-rich phase D in this pressure range, we observe that the  $a$ -axis is more compressible than the  $c$ -axis (Table 2), despite the difference between the two axial moduli ( $M_{a0} = 539$  GPa and  $M_{c0} = 421$  GPa) being smaller than in Mg-phase D ( $M_{a0} = 546$ – $669$  GPa and  $M_{c0} = 322$ – $326$  GPa) (Rosa et al. 2013; Wu et al. 2016) and Fe,Al-bearing Mg-phase D ( $M_{a0} = 545$ – $634$  GPa and  $M_{c0} = 216$ – $326$  GPa) (Chang et al. 2013; Wu et al. 2016). In fact, although the room pressure value of the  $c/a$  ratio for Fe-bearing Al-phase D is similar to those reported in previous studies for Fe-bearing Mg-phase D samples, this changes by only 0.8% upon compression from room pressure to 38 GPa (0.904 to 0.897), which is much smaller than values of  $\sim 2.2$  and  $\sim 3.3\%$  determined for pure and Fe-bearing Mg-phase D, respectively (Frost and Fei 1999; Litasov et al. 2008; Hushur et al. 2011; Chang et al. 2013; Rosa et al. 2013; Wu et al. 2016). A possible reason for these two different behaviors is that all cation sites in Al-phase D are at least partially occupied and are geometrically more regular than in Mg-phase D (Online

**TABLE 2.** Fit parameters of third-order Birch-Murnaghan, Vinet, and spin-crossover equations of state for Fe-bearing Al-phase D

EOS type	$P$ range (GPa)	$V_0$ ( $\text{\AA}^3$ )	$K_{T0}$ (GPa)	$K'_{T0}$	$a_0$ ( $\text{\AA}$ )	$M_{c0}$ (GPa)	$M'_{c0}$	$c_0$ ( $\text{\AA}$ )	$M_{c0}$ (GPa)	$M'_{c0}$
<b>Low-spin state EOS</b>										
BM3	0–38	83.68(2)	166.3(15)	4.46(12)	4.7460(9)	539(10)	12.6(7)	4.2904(3)	421(4)	15.1(3)
BM3	0–38	<i>83.689<sup>a</sup></i>	165.8(10)	4.49(9)	<i>4.7469<sup>a</sup></i>	531(6)	12.5(6)	<i>4.2891<sup>a</sup></i>	431(4)	14.5(4)
BM3	0–38	83.703 <sup>b</sup>	164.9(10)	4.53(10)	4.7465 <sup>b</sup>	536(6)	12.3(6)	4.2900 <sup>b</sup>	424(3)	14.9(4)
Vinet	0–38	83.68(2)	165.5(15)	4.62(12)	4.7460(8)	537(10)	13.0(7)	4.2905(3)	418(3)	15.7(3)
Vinet	0–38	<i>83.689<sup>a</sup></i>	165.2(10)	4.64(9)	<i>4.7469<sup>a</sup></i>	530(7)	12.9(7)	<i>4.2891<sup>a</sup></i>	428(4)	15.1(4)
Vinet	0–38	83.703 <sup>b</sup>	164.3(10)	4.69(10)	4.7465 <sup>b</sup>	534(7)	12.6(7)	4.2900 <sup>b</sup>	422(3)	15.5(4)
<b>Spin-crossover EOS</b>										
EOS type	$P$ range (GPa)	$V_0$ ( $\text{\AA}^3$ )	$K_{T0}$ (GPa)	$K'_{T0}$	$\Delta_0$	$B_0$	$\delta$	$b = c$	$C/B$	
BM3+SC	0–53	83.71(2)	161(2)	5.2(2)	14750	627(6)	2.5(2)	–2	4.73	
BM3+SC	0–53	<i>83.689<sup>a</sup></i>	161.0(12)	5.23(18)	14750	627(6)	2.53(14)	–2	4.73	
BM3+SC	0–53	83.703 <sup>b</sup>	161.0(13)	5.15(18)	14750	626(5)	2.50(14)	–2	4.73	

Notes: Values in italics were fixed in the fit.

<sup>a</sup> Fixed to the value determined at room pressure at the beamline P02.2.

<sup>b</sup> Fixed to the value determined at room pressure in house using the 8-position centering method.

Materials<sup>1</sup> Fig. S1b-c), which can lead to a less anisotropic compression mechanism of the two interstitial layers relative to Mg-rich compositions, where nominally vacant sites exist, and Mg and Si cations occupy different layers (Online Materials<sup>1</sup> Fig. S1a).

A large number of experimental studies were aimed at constraining the compression behavior of pure and Fe,Al-bearing Mg-phase D (Table 3; Online Materials<sup>1</sup> Fig. S2). Our results show that the bulk modulus of Fe-bearing Al-phase D falls toward the higher boundary of the range of values proposed for Mg-phase D (143–168 GPa) (Frost and Fei 1999; Hushur et al. 2011; Rosa et al. 2012, 2013). Only one study (Wu et al. 2016) reports a much higher bulk modulus of 179(1) GPa, which is likely related to the use of a second-order BM EOS (i.e.,  $K'_{T0} = 4$ ) to fit the data. In contrast, all other studies suggest that Mg-phase D, as well as Fe-bearing Mg-phase D have a first pressure derivative larger than 4. The lower values of  $K_{T0}$  for Mg-phase D are confirmed by a single-crystal X-ray diffraction

study (Rosa et al. 2013) and a single-crystal Brillouin scattering study (Rosa et al. 2012) on Mg-phase D samples with very similar compositions that reported consistent values of  $K_{T0} = 151(1)$  and  $K'_{T0} = 149(3)$  GPa, respectively. Xu et al. (2020) recently determined the pressure and temperature dependence of the sound velocities of Al-bearing Mg-phase D by ultrasonic interferometry and synchrotron X-ray powder diffraction, suggesting that Al incorporation in phase D decreases the bulk modulus of Mg-phase D at ambient conditions. Note, however, that when the tradeoff between  $K_{T0}$  and  $K'_{T0}$  is taken into account, the range of values determined for phase D in previous studies (Litavov et al. 2007, 2008; Chang et al. 2013; Rosa et al. 2013; Wu et al. 2016; Xu et al. 2020) falls in a relatively narrow range (Online Materials<sup>1</sup> Fig. S2). As a consequence, the range of  $K_T$  values becomes inevitably smaller with increasing pressure and results in a much weaker compositional effect on the elasticity of phase D solid solutions at the mantle transition zone and lower mantle pressures.

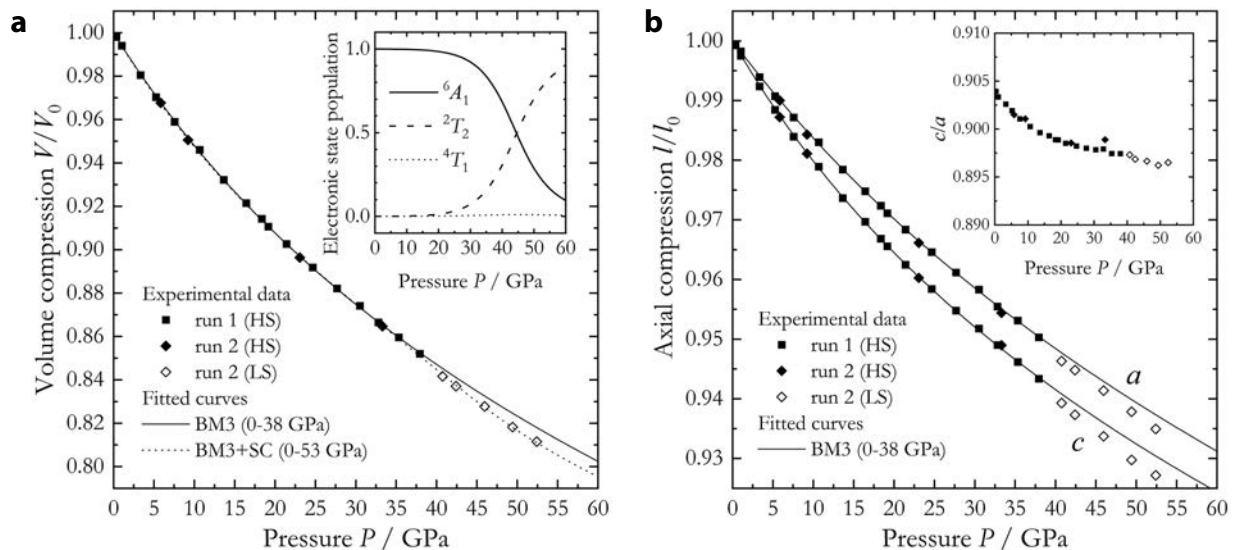


**FIGURE 3.** Volume (a) and axial (b) compression data of Fe-bearing Al-phase D collected over two separate runs. Solid squares and diamonds represent the high-spin phase, while open diamonds represent the low-spin phase. Error bars are not shown as they are smaller than the symbols. Solid lines represent third-order Birch-Murnaghan (BM3) equations of state (EOS) fits between 0 and 38 GPa, while the dashed line in a indicates the modified BM3 EOS fit of all data accounting for the spin-crossover of Fe<sup>2+</sup>. In the inset in a, the population of the three most relevant electronic states is modeled as a function of pressure based on the crystal field parameters used to fit the  $P$ - $V$  data. The inset in b shows that the  $c/a$  ratio of Fe-bearing Al-phase D only slightly decreases with pressure and is barely affected by the onset of the spin crossover.

**TABLE 3.** Fit parameters of Birch-Murnaghan equations of states of phase-D solid solutions from the present and previous studies

Composition	$V_0$ (Å <sup>3</sup> )	$K_{T0}$ (GPa)	$K'_{T0}$	$P$ range (GPa)	Method	Reference
Mg <sub>1.11</sub> Si <sub>1.6</sub> O <sub>6</sub> H <sub>3.6</sub>	85.66(1)	166(3)	4.1(3)	0–30	XRPD in DAC	Frost and Fei (1999)
Mg <sub>1.0</sub> Si <sub>1.7</sub> O <sub>6</sub> H <sub>3.0</sub>	85.1(2)	168(9)	4.3(5)	0–56	XRPD in DAC	Hushur et al. (2011)
Mg <sub>1.0</sub> Si <sub>1.7</sub> O <sub>6</sub> H <sub>3.0</sub>	85.4(3)	150(9)	5.5(4)	0–30	XRPD in DAC	Hushur et al. (2011)
Mg <sub>1.1</sub> Si <sub>1.9</sub> O <sub>6</sub> H <sub>2.4</sub>	85.6(2)	149(3)	–	0	BS	Rosa et al. (2012)
Mg <sub>1.00</sub> Fe <sub>0.11</sub> Al <sub>0.03</sub> Si <sub>1.90</sub> O <sub>6</sub> H <sub>2.50</sub>	85.1(2)	153(4)	–	0	BS	Rosa et al. (2012)
Mg <sub>0.89</sub> Fe <sub>0.14</sub> Al <sub>0.25</sub> Si <sub>1.56</sub> O <sub>6</sub> H <sub>2.93</sub>	86.10(5)	137(3)	6.3(3)	0–30	XRPD in LVP	Litasov et al. (2007)
Mg <sub>0.99</sub> Fe <sub>0.12</sub> Al <sub>0.09</sub> Si <sub>1.75</sub> O <sub>6</sub> H <sub>2.51</sub>	85.32 (2)	142(3)	6.2(4)	0–20	XRPD in LVP	Litasov et al. (2008)
Mg <sub>1.1</sub> Si <sub>1.8</sub> O <sub>6</sub> H <sub>2.5</sub>	85.80(5)	151.4(1.2)	4.89(8)	0–65	SCXRD in DAC	Rosa et al. (2013)
Mg <sub>1.00</sub> Fe <sub>0.15</sub> Al <sub>0.09</sub> Si <sub>1.75</sub> O <sub>6</sub> H <sub>2.51</sub>	86.14(3)	147(2)	6.3(3)	0–40	SCXRD in DAC	Chang et al. (2013)
Mg <sub>1.14</sub> Si <sub>1.73</sub> O <sub>6</sub> H <sub>2.81</sub>	85.07(4)	179(1)	4	0–80	SCXRD in DAC	Wu et al. (2016)
Mg <sub>0.89</sub> Fe <sub>0.11</sub> Al <sub>0.37</sub> Si <sub>1.55</sub> O <sub>6</sub> H <sub>2.65</sub>	85.7(1)	169(2)	4	0–37	SCXRD in DAC	Wu et al. (2016)
Mg <sub>0.83</sub> Al <sub>0.66</sub> Si <sub>1.20</sub> O <sub>6</sub> H <sub>2.89</sub>	86.71	143(4)	5.8(7)	0–25	XRPD in LVP	Xu et al. (2020)
Mg <sub>0.83</sub> Al <sub>0.66</sub> Si <sub>1.20</sub> O <sub>6</sub> H <sub>2.89</sub>	86.71	144(5)	5.5(7)	0–25	UI in LVP	Xu et al. (2020)
Fe <sub>0.22</sub> Al <sub>1.53</sub> Si <sub>0.86</sub> O <sub>6</sub> H <sub>3.33</sub>	83.68(2)	166.3(1.5)	4.46(12)	0–38	SCXRD in DAC	this study (BM3)

Notes: Numbers in italics were fixed in the fitting procedure. XRPD = powder X-ray diffraction. BS = Brillouin spectroscopy. SCXRD = single-crystal X-ray diffraction. UI = ultrasonic interferometry. DAC = diamond anvil cell. LVP = large-volume press.

### Spin crossover in Fe-bearing Al-phase D

When Fe<sup>2+</sup> and/or Fe<sup>3+</sup> are incorporated in phase D, they are known to undergo a high-spin (HS) to low-spin (LS) crossover in the pressure interval ranging between approximately 40 and 70 GPa, as revealed by X-ray emission spectroscopy (XES) (Chang et al. 2013) and synchrotron Mössbauer spectroscopy (SMS) (Wu et al. 2016) observations. Wu et al. (2016) determined that the fraction of Fe<sup>2+</sup> present in their sample is approximately 60%, corresponding to 0.07 Fe<sup>2+</sup> atoms per formula unit, which is believed to induce the sharp volume collapse of 1.7% observed by X-ray diffraction in a few GPa interval at approximately 40 GPa. A second drop in the unit-cell volume (2%) at approximately 65 GPa was linked to the spin crossover of Fe<sup>3+</sup>, which was also present in their sample. On the other hand, Chang et al. (2013) analyzed a phase D sample having less than 0.01 Fe<sup>2+</sup> per formula unit and observed a smooth continuous decrease both in the unit-cell volume by X-ray diffraction and in the Fe<sup>3+</sup> high-spin component by XES from 40 to 70 GPa. In this study, we observed a smooth and progressive deviation of the unit-cell volume,  $V$ , and lattice parameters  $a$  and  $c$  from the extrapolation of their respective equations of state determined using the data up to 38 GPa, i.e., below the region at which the spin crossover may occur. Owing to the similar Fe<sup>3+</sup>/ΣFe ratio of our Fe-bearing Al-phase D with that of the sample studied by Chang et al. (2013), we also interpret the volume decrease above 38 GPa as the onset of Fe<sup>3+</sup> spin crossover, suggesting that the Mg<sup>2+</sup> + Si<sup>4+</sup> = 2Al<sup>3+</sup> substitution has little to no effect on the spin crossover pressure of Fe<sup>3+</sup> in phase D.

The number of data points collected after the onset of the spin crossover (i.e., above 38 GPa) is limited and does not allow for refinement of separate EOS parameters for the Fe-bearing Al-phase D sample in the high- and low-spin states. However, a fit of all data points (i.e., before and across the spin crossover) can be obtained using a new semi-empirical formalism that has been recently proposed by Buchen (2021). In this formalism, the contribution of the spin crossover to the elastic energy (and thus to pressure) is obtained from the volume dependency of crystal-field parameters such as the crystal-field splitting  $\Delta$  and the Racah parameters  $B$  and  $C$ :

$$\Delta = \Delta_0 \left( \frac{V_0}{V} \right)^{\frac{\delta}{3}}, B = B_0 \left( \frac{V_0}{V} \right)^{\frac{b}{3}}, C = C_0 \left( \frac{V_0}{V} \right)^{\frac{c}{3}} \quad (1)$$

where the zero in the subscript denotes parameters at room pressure. The total Helmholtz free energy ( $F$ ) at a given volume is then calculated by summing the elastic energy obtained from the finite strain equation (i.e., BM3 EOS in this case), the energies associated with the three most populated electronic states (i.e.,  ${}^6A_1$ ,  ${}^2T_2$ , and  ${}^4T_1$  for Fe<sup>3+</sup>) according to the equations proposed by Tanabe and Sugano (1954), and a term accounting for configurational entropy, spin multiplicity and degeneracy of the electronic states (Buchen 2021). Finally, pressure is calculated by differentiating the total Helmholtz free energy relative to volume as  $P = -(\partial F/\partial V)_T$ . This strategy has the advantage that only one set of  $V_0$ ,  $K_{T0}$ , and  $K'_{T0}$  needs to be determined for the high-spin state, the low-spin state, and the mixed-spin region, while the electronic contribution to the spin-crossover equation is calculated separately. Buchen (2021) further showed that a good fit to the experimentally measured  $P$ - $V$  data can be obtained even when most of these parameters, such as  $\Delta_0$ ,  $b$ , and  $c$ , are fixed to values determined by previous studies for octahedrally coordinated Fe<sup>2+</sup> and Fe<sup>3+</sup> cations in other compounds, while only  $B_0$  and  $\delta$  are refined. Following the examples provided by Buchen (2021), we assumed  $C/B$  to be constant and equal to 4.73, which implies  $c = b$ , with  $b = -2$  [as Fe<sup>3+</sup> in CF-type aluminous phase, Buchen (2021)] and  $\Delta_0 = 14750 \text{ cm}^{-1}$  [as Fe<sup>3+</sup> in corundum (Lehmann and Harder 1970; Helms and Mullen 1971)], while  $B_0$  and  $\delta$  were refined. The resulting fit parameters are reported in Table 2, and the fit to the experimental data points is shown in Figure 3a. The EOS curve interpolates well the data points in both the high-spin state region and across the spin crossover, while the population density of the high-spin and low-spin electronic states, shown in the inset of Figure 3a, confirms that the transition is broad and takes place over a pressure interval of more than 30 GPa, as was previously observed by Chang et al. (2013). Note also that the room pressure values  $V_0$ ,  $K_{T0}$ , and  $K'_{T0}$  obtained from this fit are in agreement with the values obtained by fitting the  $P$ - $V$  data only up to 38 GPa (Table 2) once the tradeoff between  $K_{T0}$  and  $K'_{T0}$  is taken into account, confirming the validity of the formalism used.

In Fe-bearing Mg-phase D, the volume drop at the spin crossover is mainly driven by a shrinking of the  $c$  lattice parameter, whereas the  $a$  lattice parameter remains almost unaffected (Chang et al. 2013; Wu et al. 2016). In Fe-bearing Al-phase D, on the other hand, we observe a smooth decrease of both the  $a$  and  $c$  axes, with the  $c/a$  ratio remaining almost constant across

the spin crossover (Fig. 3b). The reason behind the different behavior shown by our sample relative to previous studies could be that, in Mg-phase D, ferric and ferrous Fe likely substitute Mg in the M1 site and not Si in the M2 site. As described above, in Mg-phase D the distance between O atoms across the interstitial layer hosting M1 is larger than that across M2, owing to the larger radius of Mg relative to Si (Online Materials<sup>1</sup> Fig. S1a). To accommodate the difference in size of the two cations, the *z* coordinates of O in Mg-phase D (Wyckoff position *6k*: *x*,0,*z*) are either larger than  $\frac{1}{4}$  or smaller than  $\frac{3}{4}$ , making the Si layer thinner than the Mg layer (Online Materials<sup>1</sup> Fig. S1a). At the spin crossover, the ionic radius of Fe decreases and thus the octahedral volume of M1 in Mg-phase D must decrease as well. This means that in order for M1 to be reduced in size while leaving M2 unaffected, the *c* lattice parameter must shrink while the *z* coordinates of O approach the value  $\frac{1}{4}$  or  $\frac{3}{4}$ . In Fe-bearing Al-phase D, this cannot happen when the hexagonal space group is considered since the *z* coordinate of the O atoms is constrained by symmetry (Wyckoff position *6g*: *x*,*x*, $\frac{1}{2}$ ) and the two interstitial layers perpendicular to the *c*-axis have the same thickness. This is likely the consequence of Al, Si, and Fe<sup>3+</sup> being more or less randomly distributed in Fe-bearing Al-phase D (Online Materials<sup>1</sup> Fig. S1c). Therefore, the octahedral volumes of the three cation sites must collapse simultaneously while the atomic coordinates of all atoms are likely to remain unchanged. The fact that we observed a simultaneous decrease of the *a* and *c* lattice parameters above 38 GPa seems to indeed confirm the hypothesis of a hexagonal space group for our sample.

Recently, Meier et al. (2022) analyzed the possible correlations between H-bond symmetrization and high-to-low spin crossover in Fe-bearing phase  $\delta$  and Fe,Al-bearing Mg-phase D by means of nuclear magnetic resonance spectroscopy (NMR), synchrotron Mössbauer spectroscopy, and X-ray diffraction. In all the samples studied by Meier et al. (2022), including the one of Fe,Al-bearing Mg-phase D, the H-bond symmetrization was found not to affect the resonance frequency of the <sup>1</sup>H nuclei, but only the width of the peak, which is related to the proton mobility. The spin crossover of Fe<sup>3+</sup>, on the other hand, was found to significantly change the resonance frequency of the <sup>1</sup>H while leaving the width of the NMR signal unaffected. These two phenomena were observed at different pressures in all the hydrous phases investigated by Meier et al. (2022), suggesting that they are not correlated. The H-bond symmetrization in the phase D sample was observed at 23(2) GPa, while the spin crossover of Fe<sup>3+</sup> was observed above 36 GPa, which is in good agreement with both our observations and the previous study of Chang et al. (2013). As the strength of H-bonds in Al-phase D samples is higher than in Mg-phase D samples (Yang et al. 1997; Boffa Ballaran et al. 2010; Pamato et al. 2015), it is reasonable to assume that the symmetrization of H-bond in Al-phase D will take place at lower pressure than in Mg-phase D. Therefore, we expect that the H-bond symmetrization and spin crossover of Fe<sup>3+</sup> in Fe-bearing Al-phase D are uncorrelated, similarly to what was observed in Fe,Al-bearing Mg-phase D by Meier et al. (2022).

### IMPLICATIONS

Previous experimental studies have shown that the wide *P-T* stability field of phase D makes it a suitable host for water in

the Earth's mantle transition zone and lower mantle (Nishi et al. 2014; Pamato et al. 2015; Liu et al. 2019). As Al is incorporated in its crystal structure, phase D can survive even at temperatures of the ambient mantle within MgO-poor Al-rich subducted basaltic crust, where water can be delivered by hydrous melts upwelling from dehydrating ultramafic lithologies within the slab (Pamato et al. 2015). Al-rich phase D was also reported to be stable in MgO-rich basaltic crust between 20 and 25 GPa (Liu et al. 2019) and to transform to a solid solution of  $\delta$ -AlOOH and DHMS phase H (MgSiO<sub>4</sub>H<sub>2</sub>) above 25 GPa. It was recently proposed that solid solutions between phase H and  $\delta$ -AlOOH contribute to the faster sound velocities of hydrous mid-ocean ridge basalt (MORB) compared with those of dry MORB at shallow lower mantle pressures, owing to their high-bulk modulus and relative low density after the H-bond symmetrization (Satta et al. 2021). These findings are particularly interesting as they suggest an intimate relationship between H-bond symmetrization and elastic stiffening of CaCl<sub>2</sub>-type oxyhydroxides at high pressure. Based on the analysis of bond valences and Pauling bond strength of our sample and that studied by Pamato et al. (2015), it seems that the H-bonds of Al-Phase D are stronger than those of Mg-phase D. Nuclear magnetic resonance (NMR) spectroscopy and single-crystal diffraction measurements on a Fe,Al-bearing Mg-phase D sample, however, showed no evidence for a shift in the resonance frequency and a change in compressibility across the H-bond symmetrization (Meier et al. 2022). Given that the H-bonds in Al-phase D and Fe-bearing Al-phase D are stronger than in Mg-phase D samples, it is reasonable to expect the H-bond symmetrization to take place below 23 GPa. However, no change in the volume and axial compressibility was observed in Fe-bearing Al-phase D between room pressure and 38 GPa. Therefore, we conclude that the strength of H-bonds alone cannot be responsible for an increase in the bulk modulus of phase D and other H-bearing minerals, but additional features, such as a change in the space group symmetry, must also occur across the H-bond symmetrization, as it was observed in the case of pure and Fe-bearing phase  $\delta$  (Sano-Furukawa et al. 2018; Ohira et al. 2019; Satta et al. 2021).

### ACKNOWLEDGMENTS

We thank Raphael Njul for preparing the samples for EPMA and Detlef Krauß for his assistance with EPMA measurements. Johannes Buchen is acknowledged for fruitful discussion on the spin-crossover equation of state and for sharing the script to fit the *P-V* data. We also thank Oliver Tschauner, Angelika D. Rosa, an anonymous reviewer, and the technical editor for their constructive comments that helped us improving the manuscript. This study was supported by DFG grant FR1555/11. We acknowledge DESY (Hamburg, Germany), a member of the Helmholtz Association HGF, for the provision of experimental facilities. Parts of this research were carried out at the Extreme Conditions Beamline P02.2, PETRA-III.

### REFERENCES CITED

- Angel, R.J. (2000) Equations of State. Reviews in Mineralogy and Geochemistry, 41, 35–59, <https://doi.org/10.2138/rmg.2000.41.2>.
- Angel, R.J. and Finger, L.W. (2011) SINGLE: A program to control single-crystal diffractometers. Journal of Applied Crystallography, 44, 247–251, <https://doi.org/10.1107/S0021889810042305>.
- Angel, R.J., Alvaro, M., and Gonzalez-Platas, J. (2014) EoSFit7c and a Fortran module (library) for equation of state calculations. Zeitschrift für Kristallographie. Crystal-line Materials, 229, 405–419, <https://doi.org/10.1515/zkri-2013-1711>.
- Bindi, L., Nishi, M., Tsuchiya, J., and Irifune, T. (2014) Crystal chemistry of dense hydrous magnesium silicates: The structure of phase H, 99, 1802–1805.
- Birch, F. (1947) Finite elastic strain of cubic crystals. Physical Review, 71, 809–824, <https://doi.org/10.1103/PhysRev.71.809>.
- Boehler, R. and De Hantsetters, K. (2004) New anvil designs in diamond-cells. High

- Pressure Research, 24, 391–396, <https://doi.org/10.1080/08957950412331323924>.
- Boffa Ballaran, T., Frost, D.J., Miyajima, N., and Heidelbach, F. (2010) The structure of a super-aluminous version of the dense hydrous-magnesium silicate phase D. *American Mineralogist*, 95, 1113–1116, <https://doi.org/10.2138/am.2010.3462>.
- Buchen, J. (2021) Seismic Wave Velocities in Earth's Mantle from Mineral Elasticity. In H. Marquardt, M. Ballmer, S. Cottar, and J. Konter, Eds., *Mantle Convection and Surface Expressions*, p. 51–95 p. American Geophysical Union.
- Chang, Y.Y., Jacobsen, S.D., Lin, J.F., Bina, C.R., Thomas, S.M., Wu, J., Shen, G., Xiao, Y., Chow, P., Frost, D.J., and others. (2013) Spin transition of Fe<sup>3+</sup> in Al-bearing phase D: An alternative explanation for small-scale seismic scatterers in the mid-lower mantle. *Earth and Planetary Science Letters*, 382, 1–9, <https://doi.org/10.1016/j.epsl.2013.08.038>.
- Frost, D.J. (2006) The stability of hydrous mantle phases. *Reviews in Mineralogy and Geochemistry*, 62, 243–271, <https://doi.org/10.2138/rmg.2006.62.11>.
- Frost, D.J. and Fei, Y. (1999) Static compression of the hydrous magnesium silicate phase D to 30 GPa at room temperature. *Physics and Chemistry of Minerals*, 26, 415–418, <https://doi.org/10.1007/s002690050202>.
- Gonzalez-Platas, J., Alvaro, M., Nestola, F., and Angel, R.J. (2016) EosFit7-GUI: A new graphical user interface for equation of state calculations, analyses and teaching. *Journal of Applied Crystallography*, 49, 1377–1382, <https://doi.org/10.1107/S1600576716008050>.
- Hamilton, W.C. (1965) Significance tests on the crystallographic R factor. *Acta Crystallographica*, 18, 502–510, <https://doi.org/10.1107/S0365110X65001081>.
- Helms, W.R. and Mullen, J.G. (1971) Study of pure and doped cobaltous and nickelous oxide. *Physical Review B, Solid State*, 4, 750–757, <https://doi.org/10.1103/PhysRevB.4.750>.
- Hübschle, C.B., Sheldrick, G.M., and Dittrich, B. (2011) ShelXle: A Qt graphical user interface for SHELXL. *Journal of Applied Crystallography*, 44, 1281–1284, <https://doi.org/10.1107/S0021889811043202>.
- Hushur, A., Manghnani, M.H., Smyth, J.R., Williams, Q., Hellebrand, E., Lonappan, D., Ye, Y., Dera, P., and Frost, D.J. (2011) Hydrogen bond symmetrization and equation of state of phase D. *Journal of Geophysical Research*, Solid Earth, 116, 1–8.
- Ishii, T., Shi, L., Huang, R., Tsujino, N., Druzhbin, D., Myhill, R., Li, Y., Wang, L., Yamamoto, T., Miyajima, N., and others. (2016) Generation of pressures over 40 GPa using Kawai-type multi-anvil press with tungsten carbide anvils. *The Review of Scientific Instruments*, 87, 024501, <https://doi.org/10.1063/1.4941716>.
- Ishii, T., Liu, Z., and Katsura, T. (2019) A breakthrough in pressure generation by a Kawai-type multi-anvil apparatus with tungsten carbide anvils. *Engineering*, 5, 434–440, <https://doi.org/10.1016/j.eng.2019.01.013>.
- Kantor, I., Prakash, V., Kantor, A., Dera, P., Kurnosov, A., Sinogeikin, S., Dubrovinskaya, N., and Dubrovinsky, L. (2012) BX90: A new diamond anvil cell design for X-ray diffraction and optical measurements. *The Review of Scientific Instruments*, 83, 125102, <https://doi.org/10.1063/1.4768541>.
- King, H.E. Jr. and Finger, L.W. (1979) Diffracted beam crystal centering and its application to high-pressure crystallography. *Journal of Applied Crystallography*, 12, 374–378, <https://doi.org/10.1107/S0021889879012723>.
- Kurnosov, A., Kantor, I., Boffa-Ballaran, T., Lindhardt, S., Dubrovinsky, L., Kuznetsov, A., and Zehnder, B.H. (2008) Anovel gas-loading system for mechanically closing of various types of diamond anvil cells. *The Review of Scientific Instruments*, 79, 045110, <https://doi.org/10.1063/1.2902506>.
- Lehmann, G. and Harder, H. (1970) Optical spectra of di- and trivalent iron in corundum. *American Mineralogist*, 55, 98–105.
- Liermann, H.P., Konôpková, Z., Morgenroth, W., Glazyrin, K., Bednarčík, J., McBride, E.E., Petitgirard, S., Deltiz, J.T., Wendt, M., Bican, Y., and others. (2015) The extreme conditions beamline P02.2 and the extreme conditions science infrastructure at PETRA III. *Journal of Synchrotron Radiation*, 22, 908–924, <https://doi.org/10.1107/S1600577515005937>.
- Litasov, K.D., Ohtani, E., Suzuki, A., and Funakoshi, K. (2007) The compressibility of Fe- and Al-bearing phase D to 30 GPa. *Physics and Chemistry of Minerals*, 34, 159–167, <https://doi.org/10.1007/s00269-006-0136-4>.
- Litasov, K.D., Ohtani, E., Nishihara, Y., Suzuki, A., and Funakoshi, K. (2008) Thermal equation of state of Al- and Fe-bearing phase D. *Journal of Geophysical Research*, Solid Earth, 113, 1–13.
- Liu, Z., Nishi, M., Ishii, T., Fei, H., Miyajima, N., Ballaran, T.B., Ohfuji, H., Sakai, T., Wang, L., Shcheka, S., and others. (2017) Phase relations in the system MgSiO<sub>3</sub>-Al<sub>2</sub>O<sub>3</sub> up to 2300 K at lower mantle pressures. *Journal of Geophysical Research*, Solid Earth, 122, 7775–7788, <https://doi.org/10.1002/2017JB014579>.
- Liu, X., Matsukage, K.N., Nishihara, Y., Suzuki, T., and Takahashi, E. (2019) Stability of the hydrous phases of Al-rich phase D and Al-rich phase H in deep subducted oceanic crust. *American Mineralogist*, 104, 64–72, <https://doi.org/10.2138/am-2019-6559>.
- Lufaso, M.W. and Woodward, P.M. (2001) Prediction of the crystal structures of perovskites using the software program SPuDS. *Acta Crystallographica*, B57, 725–738, <https://doi.org/10.1107/S0108768101015282>.
- McCammon, C.A. (1994) A Mössbauer milliprobe: Practical considerations. *Hyperfine Interactions*, 92, 1235–1239, <https://doi.org/10.1007/BF02065761>.
- Meier, T., Trybel, F., Khandarkhaeva, S., Laniel, D., Ishii, T., Aslundukova, A., Dubrovinskaya, N., and Dubrovinsky, L. (2022) Structural independence of hydrogen-bond symmetrisation dynamics at extreme pressure conditions. *Nature Communications*, 13, 3042, <https://doi.org/10.1038/s41467-022-30662-4>.
- Nishi, M., Irifune, T., Tsuchiya, J., Tange, Y., Nishihara, Y., Fujino, K., and Higo, Y. (2014) Stability of hydrous silicate at high pressures and water transport to the deep lower mantle. *Nature Geoscience*, 7, 224–227, <https://doi.org/10.1038/ngeo2074>.
- OHIRA, I., Ohtani, E., Sakai, T., Miyahara, M., Hirao, N., Ohishi, Y., and Nishijima, M. (2014) Stability of a hydrous  $\delta$ -phase, AlOOH-MgSiO<sub>3</sub>(OH)<sub>2</sub>, and a mechanism for water transport into the base of lower mantle. *Earth and Planetary Science Letters*, 401, 12–17, <https://doi.org/10.1016/j.epsl.2014.05.059>.
- OHIRA, I., Jackson, J.M., Solomatova, N.V., Sturhahn, W., Finkelstein, G.J., Kamada, S., Kawazoe, T., Maeda, F., Hirao, N., Nakano, S., and others. (2019) Compressional behavior and spin state of  $\delta$ -(Al,Fe)OOH at high pressures. *American Mineralogist*, 104, 1273–1284, <https://doi.org/10.2138/am-2019-6913>.
- Ohtani, E., Amaike, Y., Kamada, S., Sakamaki, T., and Hirao, N. (2014) Stability of hydrous phase H MgSiO<sub>3</sub>H<sub>2</sub> under lower mantle conditions. *Geophysical Research Letters*, 41, 8283–8287, <https://doi.org/10.1002/2014GL061690>.
- Pamato, M.G., Myhill, R., Boffa Ballaran, T., Frost, D.J., Heidelbach, F., and Miyajima, N. (2015) Lower-mantle water reservoir implied by the extreme stability of a hydrous aluminosilicate. *Nature Geoscience*, 8, 75–79, <https://doi.org/10.1038/ngeo2306>.
- Prescher, C., McCammon, C., and Dubrovinsky, L. (2012) MossA: A program for analyzing energy-domain Mössbauer spectra from conventional and synchrotron sources. *Journal of Applied Crystallography*, 45, 329–331, <https://doi.org/10.1107/S0021889812004979>.
- Ralph, R.L. and Finger, L.W. (1982) A computer-program for refinement of crystal orientation matrix and lattice-constants from diffractometer data with lattice symmetry constraints. *Journal of Applied Crystallography*, 15, 537–539, <https://doi.org/10.1107/S0021889882012539>.
- Rosa, A.D., Sanchez-Valle, C., and Ghosh, S. (2012) Elasticity of phase D and implication for the degree of hydration of deep subducted slabs. *Geophysical Research Letters*, 39, L06304, <https://doi.org/10.1029/2012GL050927>.
- Rosa, A.D., Mezouar, M., Garbarino, G., Bouvier, P., Ghosh, S., Rohrbach, A., and Sanchez-Valle, C. (2013) Single-crystal equation of state of phase D to lower mantle pressures and the effect of hydration on the buoyancy of deep subducted slabs. *Journal of Geophysical Research*, Solid Earth, 118, 6124–6133, <https://doi.org/10.1002/2013JB010060>.
- Sano-Furukawa, A., Kagi, H., Nagai, T., Nakano, S., Fukura, S., Ushijima, D., Iizuka, R., Ohtani, E., and Yagi, T. (2009) Change in compressibility of  $\delta$ -AlOOH and  $\delta$ -AlOOD at high pressure: A study of isotope effect and hydrogen-bond symmetrisation. *American Mineralogist*, 94, 1255–1261, <https://doi.org/10.2138/am.2009.3109>.
- Sano-Furukawa, A., Hattori, T., Komatsu, K., Kagi, H., Nagai, T., Molaison, J.J., Dos Santos, A.M., and Tulk, C.A. (2018) Direct observation of symmetrisation of hydrogen bond in  $\delta$ -AlOOH under mantle conditions using neutron diffraction. *Scientific Reports*, 8, 15520, <https://doi.org/10.1038/s41598-018-33598-2>.
- Satta, N., Criniti, G., Kurnosov, A., Boffa Ballaran, T., Ishii, T., and Marquardt, H. (2021) High-pressure elasticity of  $\delta$ -(Al,Fe)OOH single crystals and seismic detectability of hydrous MORB in the shallow lower mantle. *Geophysical Research Letters*, 48, 1–10, <https://doi.org/10.1029/2021GL094185>.
- Sheldrick, G.M. (2015a) Crystal structure refinement with SHELXL. *Acta Crystallographica*, C71, 3–8, <https://doi.org/10.1107/S2053229614024218>.
- (2015b) Foundations and advances SHELXT-integrated space-group and crystal-structure determination. *Acta Crystallographica*, 71, 3–8.
- Shen, G., Wang, Y., Dewaele, A., Wu, C., Fratanduono, D.E., Eggert, J., Klotz, S., Dziubek, K.F., Loubeyre, P., Fat'yanov, O.V., and others. (2020) Toward an international practical pressure scale: A proposal for an IPPS ruby gauge (IPPS-Ruby2020). *High Pressure Research*, 40, 299–314, <https://doi.org/10.1080/08957959.2020.1791107>.
- Tanabe, Y. and Sugano, S. (1954) On the absorption spectra of complex ions. I. *Journal of the Physical Society of Japan*, 9, 753–766, <https://doi.org/10.1143/JPSJ.9.753>.
- Vinet, P., Rose, J.H., Ferrante, J., and Smith, J.R. (1989) Universal features of the equation of state of solids. *Journal of Physics Condensed Matter*, 1, 1941–1963, <https://doi.org/10.1088/0953-8984/1/11/002>.
- Wu, X., Wu, Y., Lin, J.-F., Liu, J., Mao, Z., Guo, X., Yoshino, T., McCammon, C., Prakash, V.B., and Xiao, Y. (2016) Two-stage spin transition of iron in FeAl-bearing phase D at lower mantle. *Journal of Geophysical Research*, Solid Earth, 121, 6411–6420, <https://doi.org/10.1002/2016JB013209>.
- Xu, C., Gréaux, S., Inoue, T., Noda, M., Sun, W., Kuwahara, H., and Higo, Y. (2020) Sound velocities of Al-bearing phase D up to 22 GPa and 1300 K. *Geophysical Research Letters*, 47, 1–10, <https://doi.org/10.1029/2020GL088877>.
- Yang, H., Prewitt, C.T., and Frost, D.J. (1997) Crystal structure of the dense hydrous magnesium silicate, phase D. *American Mineralogist*, 82, 651–654, <https://doi.org/10.2138/am-1997-5-627>.

MANUSCRIPT RECEIVED APRIL 20, 2022

MANUSCRIPT ACCEPTED OCTOBER 25, 2022

ACCEPTED MANUSCRIPT ONLINE NOVEMBER 3, 2022

MANUSCRIPT HANDLED BY OLIVER TSCHAUNER

## Endnote:

<sup>1</sup>Deposit item AM-23-98559. Online Materials are free to all readers. Go online, via the table of contents or article view, and find the tab or link for supplemental materials. The CIF has been peer-reviewed by our Technical Editors.